TERRAIN-ADAPTIVE GROUND FILTERING OF AIRBORNE LIDAR DATA BASED ON SALIENCY-AWARE THIN PLATE SPLINE

X. Liu [a], Y. Zhang [a, *], X. Huang[a], Y. Wan[a], Y. Zhang[b], S. Wang[c]

[a] School of Remote Sensing and Information Engineering, Wuhan University, 430079 Wuhan, China –
(liuxy0319, zhangyj, 2013302590106, yi.wan)@whu.edu.cn
[b] Huawei Tech. Co., Ltd., Wuhan, China – zhangyanfeng8@huawei.com
[c] Institute of Spacecraft System Engineering, China Academy of Space Tech., 100094 Beijing, China – rswangsiheng@163.com

Commission II, WG II/3

KEY WORDS: Ground Filtering, Airborne LiDAR, Saliency Division, Surface Interpolation, Thin-Plate-Spline, Relative Variation Coefficient

ABSTRACT:

Ground filtering separates the ground and non-ground points from point clouds, which is the essential process for DEM generation, semantic segmentation, model reconstruction and so forth. Considering the topologically complex terrain environments, the segmentation results are prone to be disturbed dealing with steep slopes, buildings, bridges, cliffs, etc. from Airborne LiDAR point clouds. In this paper, a saliency-aware Thin-Plate-Spline (SATPS) interpolation method is proposed including two steps: saliency division and adaptive regularized TPS interpolation with relative variance coefficient. Firstly, the point clouds are indexed in 2D grids and segments are clustered step probing toward 8-adjacent scanning directions. Then, the saliency of each grid is calculated according to the elevation variance of adjacent segments towards each scanning direction. Subsequently, grids of high ground saliency are considered as candidates for seed point selection and then clustered by region growing. The TPS surface is interpolated for each cluster loosely fitting to the seed points involving an adaptive relative variance coefficient which is according to ground saliency and elevation deviation. And finally, the ground points are extracted around the TPS surface. Experimental results indicate that the proposed SATPS algorithm achieves better Type 1 accuracy and total accuracy than the state-of-the-art algorithms in scenes with complex terrain structures, which is practical to generate DEM products.

1. INTRODUCTION

Ground filtering is one of the most essential and foundational processes for urban mapping applications using point clouds, which plays an important role in DEM generation, model reconstruction, classification, object extraction, etc. Although relevant researches have been carried out for decades, it is obstinate to separate ground and non-ground points from LiDAR (Light Detection and Ranging) point clouds efficiently with high accuracy due to the uneven sampling density and the complicated terrain structures both in the urban scenes and mountainous areas.

Filtering methods for three major categories of LiDAR platforms vary due to the different viewing angle and sampling density (Roberts et al., 2019). Terrestrial Laser Scanning (TLS) and Mobile Laser Scanning (MLS) are ground-based platforms, static and moving respectively, the filtering strategies of which focus on the scan-line analysis and neighborhood analysis (Martínez Sánchez et al., 2019; Che et al., 2017). The capturing distance of Airborne Laser Scanning (ALS) is relatively consistent and the sampling density is much sparser. Considering limitation of scanning degree and flight elevation, ALS point clouds are commonly processed as 2.5D data for filtering and typical methods mainly include mathematical morphology (Li et al., 2013; Li et al., 2017; Meng et al., 2019), surface interpolation (Hu et al., 2014), segmentation (Chen et al., 2016), etc., which are discussed in this paper.

Since filtering is also a semantic segmentation task, machine learning methods classify the point clouds by trained classifiers

(Wang et al., 2015; Liu et al., 2019), including Information Vector Machine, Relevance Vector Machine, and Random Forest, etc. Deep learning-based methods sprung up as the neural networks towards point clouds processing became mature. Except for point clouds-based networks such as the PointNet (Qi et al., 2017), image-based methods (Yilmaz et al., 2018) are also applied since LiDAR along with multi-view images or photogrammetric point clouds from UAV photos (Gruszczyński et al., 2019; Zeybek and Şanlıoğlu, 2019) became feasible.

Surface interpolation-based methods extract the bare earth by fitting piece-wise successive surfaces for local patches. Triangular Irregular Networks (TIN) are reconstructed and iteratively densified to obtain the ground surface in classic pipelines (Zhao et al., 2016). Considering the uneven density of point clouds, Ma and Li (2019) resort to 3D alpha shapes based on ball-pivoting to generate 3D TINs. Curved surface-based methods perform better to preserve sharp details and conform terrain relief. Least-square, Thin-Plate-Spline (TPS) (Meng et al., 2019), and scanline spline (Martínez Sánchez et al., 2019) are commonly used to fit the surface while accurate interpolation points are strictly required for reasonable fitting. Improvements involve seed point selection such as moving-window weighted iterative least-squares fitting (Qin et al., 2017). Cheng et al. (2019) extended the TPS algorithm by improved skewness balancing. The state-of-the-art cloth simulation algorithm (Zhang et al., 2016) covers the surface inverted from points using a rigid cloth, which is easy-to-use and widely applied. However, the lack of explicit structures and the noise of point clouds make it a

---

* Corresponding author

challenge to fit and accurately determine the segmentation surface for all categories of terrains.

To deal with topographically complex terrain environment, including steep slopes, multi-layer buildings, and cliffs, etc., researchers proposed solutions aimed at adaptive parameter settings for multitudinous terrains (Mongus and Žalik, 2012). Adaptive slope parameters (Susaki, 2012) are frequently optimized. Wan et al. (2018) resorted to the terrain relief index for tuning slope-related parameters. Considering density variance, scholars changed the iterative judgment criteria (Nie et al., 2017) to improve progressive TIN-based methods to decrease type I error (Dong et al., 2018; Zhao et al., 2016). Intrinsic structures of certain terrains are researched particularly and multi-scale filtering is conducted to preserve break lines (Yang et al., 2016). In addition, the ground and non-ground separation can be cast as a binary labeling problem and graph-cuts can be used to obtain a global optimized solution (He et al., 2018). On this basis, Hu et al. (2015) proposed the semi-global filtering method and balanced the energy function by adaptive ground saliency to adapt to discontinuous terrains.

In this paper, a terrain-adaptive ground filtering method is proposed based on saliency division and TPS interpolation. The workflow of the proposed SATPS method is shown in Figure 1. The point clouds are firstly indexed by 2D grids, which are clustered according to terrain saliency analysis, and then the regularized TPS is conducted towards clustered grids to determine the filtering surface. The contributions of this paper mainly consist of:
1. A saliency division method to select candidate ground grids and seed points for TPS interpolation;
2. An adaptive coefficient for the regularized item in TPS interpolation to loosen the seed points constraints.
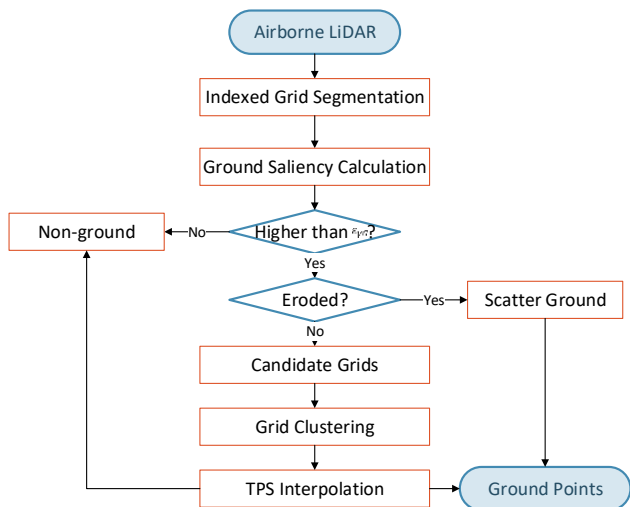

Figure 1. The workflow of this paper

2. SALIENCY DIVISION

The ground saliency (Hu et al., 2015) is an index to reveal the probability of a grid as ground according to the elevation varies for local point neighbors with a range of 0-1. Simply put, The larger the value, the higher the possibility that the point is a ground point. Considering the efficiency, the point clouds are rasterized in a regularized 2D grid to calculate the ground saliency.

2.1 Grid Segmentation

The point clouds are firstly indexed by a regularized grid in 2D and for each $d \times d$ grid, we assume the lowest elevation as the elevation of the grid. Step probing is conducted to divide grids if distinct height differences exist. And adjacent grids with similar elevations are merged. The probing is conducted scanning towards 8 directions for each grid. For example, starting from the grid g_{ij}, along the scanning direction, assume the current grid is g_{cur} and the next grid is g_{next}. If the elevation difference of g_{ij} and g_{next} is larger than ε_h, or g_{next} is empty, cluster grids from the starting grid g_{ij} to the current grid g_{cur} as one segment. And subsequently, starting from the next non-void grid to continue probing. Figure 2 illustrates a segmentation progress of the probing: along the scanning direction, points which are continuous in the horizontal direction and close in the elevation are divided into the same segment, then the grids are segmented into 4 segments caused by the elevation different higer than ε_h and the blank region. To ensure that each grid contains only one segment, grid g_{ij} is partitioned to 4x4 sub-grids and the same step probing process is conducted to detect sub-segments. If a grid g_{ij} contains n_k ($n_k \geq 1$) sub-segments, the grid is duplicated n_k times and n_k sub-segments are assigned to duplicated grids respectively. Mark each grid with the separation as:

$$K(i,j) = \{g_{ij}^k | g_{ij}^k \subseteq g_{ij}\}, k = 1,2,\cdots,n_k \qquad (1)$$

where g_{ij}^k is the kth duplicated grid of g_{ij}.

(a) Grid indexing   (b) Scanning directions

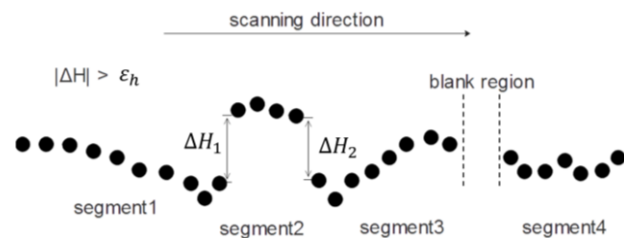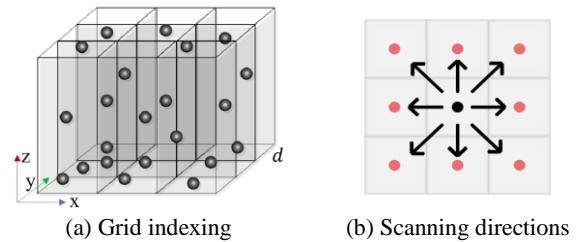(c) Scanning process for one of the directions
Figure 2. Grid segmentation

2.2 Ground Saliency Calculation

The saliency calculation by single scanning direction is based on the segments. And the saliency of each grid is the superposition of 8 scanning directions.

The ground saliency of the non-void grid is initialized as 1. Scanning towards 8 directions and along each scanning direction, if the difference between the end grid of the current segment and the start grid of the next segment is larger than ε_h, the saliency of grids in the current segment is decreased by 1. Traverse all the directions to obtain the aggregated saliency of each grid: if grids of a segment are higher than surrounding adjacent grids, the ground saliency will be 0 otherwise the value will be 1. The equation of ground saliency calculation is formed as:

$$\forall k \leq \#K(i,j), \gamma(i,j)_k = 1 - \frac{\sum_{d \in D(i,j)}[\Delta H > \varepsilon_h]}{\#D(i,j)} \quad (2)$$

$$\Delta H = H\left(Seg_{m|d}^E\right) - H\left(Seg_{m+1|d}^S\right) \quad (3)$$

$$Saliency(i,j) = \frac{\sum_{k=1}^{k<\#K(i,j)} \gamma(i,j)_k}{\#K(i,j)} \quad (4)$$

where $\gamma(i,j)_k$ is saliency of g_{ij}^k. $D(i,j)$ represents the scanning directions to calculate g_{ij}^k. $H(\cdot)$ represents the absolute elevation value (in meter) of the segment and m is the segment index. In direction d, g_{ij}^k belongs to segment $Seg_{m|d}$. Seg_m^S and Seg_m^S are starting grid and end grid of Seg_m respectively. $[\cdot]$ equals to 1 if the argument is true or 0 if false. Notably, as shown in Figure 3, among three downwards steps, the 2nd is skipped for the calculation of Seg_4 since Seg_5 contains only 1 grid, and the 3rd step condition is passed to Seg_4.
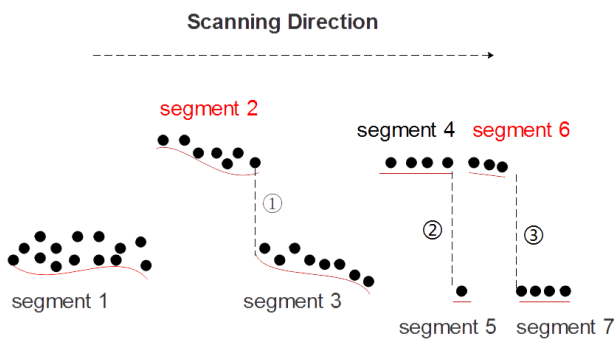
Scanning Direction

Figure 3. Ground saliency calculation

Saliency for particular terrains is optimized and discussed taking the building as an example. Grids of a building are generally higher than the adjacent grids whereas the buildings with sunken holes may break the rules. To repair the abnormal saliency, the morphological erosion process is conducted to grids whose saliency is higher than $\varepsilon_{\gamma s}$. Grids that eliminated by corrosion are marked as *Scatter Ground*, which will be excluded during the surface fitting but will be still considered as ground grids if they lie on the surrounding surface. Figure 4 shows the point clouds rendered by elevation (the strips in the pictures are caused by higher point clouds density) and the corresponding ground saliency.
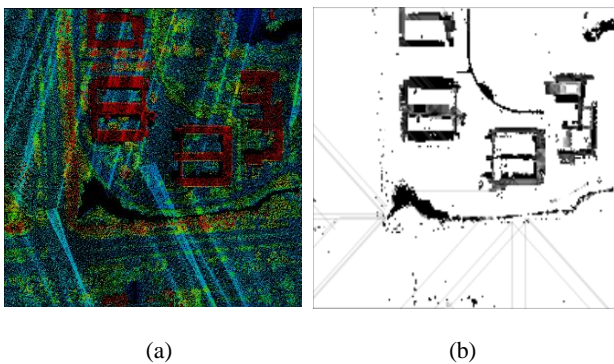

(a)   (b)

Figure 4. Point clouds rendering of elevation and ground saliency. (a) the original point clouds rendered by elevation (blue for the lower while red for the higher); (b) the grid rendered by saliency (black for 0 while white for 1)

The black area in Figure 4b includes the point cloud holes, the roofs of the buildings and the lower part of a small amount of

dense vegetation. Due to the lack of ground points, the ground saliency values of these area are close to or equal to 0; the ground saliency values of the point cloud in the flat ground area are close to or equal to 1.0. Ground saliency values in other areas are generally between 0 and 1.0.

However, the ground saliency can only be the reference for ground points determination. Taken a building area shown in Figure 5 as example, the ground saliency of the sunkun part is higher but it is actually the inner part of the building. Morphological method can be utilized to revise the saliency to some extent but the substantive filtering issues cannot be resolved. The extraction of the ground surface will be discussed in the next section.
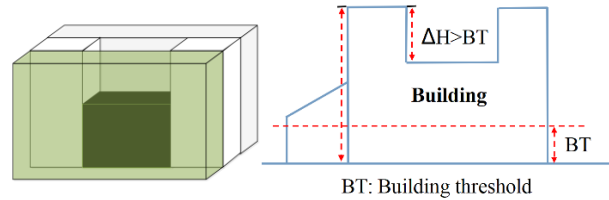
(a) Building structure with sunken parts
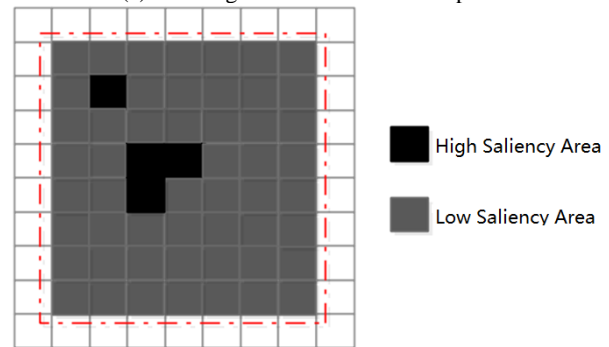
(b) Ground saliency of a building area
Figure 5. Saliency optimization for particular terrains

3. SURFACE INTERPOLATION

Since TPS is sensitive to the seed points, it is crucial to select reasonable groups of seed points, which should be interrupted by steps and steep slopes. In this section, the selection of seed points is based on the saliency calculated in the last section, and an optimized TPS interpolation is proposed to adapt to complex terrains.

3.1 Selection of Ground Seed Point

For grid g_{ij} (not marked as *Scatter*), if $Saliency(i,j) > \varepsilon_{\gamma G}$, is considered as the candidate grid for ground seed point selection. Candidate grids are clustered based on region growing which conforms the following conditions:

$$z - z_{adj} < \varepsilon_z \quad (5)$$

$$\frac{\left(x - x_{adj}\right)^2 + \left(y - y_{adj}\right)^2}{\left(z - z_{adj}\right)^2} < \varepsilon_{slope} \quad (6)$$

where   x, y, z = coordinates of the current grid;
$x_{adj}, y_{adj}, z_{adj}$ = coordinates of 8-adjacent grid;
ε_z, ε_{slope} = thresholds for elevation (in meter) and slope ratio.

For grid that is split into several sub-grids, i.e., $\#K(i,j) > 1$, points in g_{ij}^k are clustered to connected adjacent grids respectively. In Figure 6, the red points have the same horizontal coordinates but with different elevation, and will be split into different sub-grids. This situation is common in multi-layer terrains, for instance, the bridges, roof eaves, cliffs, etc., while the traditional 2.5D ground filtering methods confuse to handle the 3D variance.
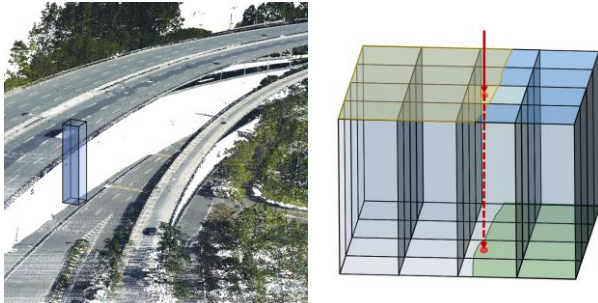

Figure 6. Multi-layer segments cluster

3.2 Regularized TPS Interpolation

Although grids are clustered for piece-wise TPS fitting, the grid height is roughly taken as the lowest elevation and the uneven sampling density leaves holes, which makes the seed points unreliable. Since the TPS fits seed points rigorously, to avoid over-fitting, an adaptive regularized item with coefficient λ is introduced according to the ground saliency. And ultimately, the ground points are extracted as points around the piece-wise TPS surface.

A seed point is the center of a candidate grid with the lowest elevation of the grid. TPS interpolation fits a smooth surface to interpolates the seed points. The TPS surface is expressed as:

$$\hat{z} = a_0 + a_1 x + a_2 y + \sum_{i=1}^{n} \omega_i K_i \tag{7}$$

where d_i is the distance, $d_i = \sqrt{(x - x_i)^2 + (y - y_i)^2}$. $\sum_{i=1}^{n} \omega_i K_i$ constrains the skewness of the surface and ensures the minimum curvature. a_0 and the weight coefficients ω_i are unknown parameters, which can be solved by Equation 8 as given by Mongus and Žalik (2012):

$$\begin{bmatrix} K & P \\ P^T & 0 \end{bmatrix} \begin{bmatrix} \omega \\ a \end{bmatrix} = \begin{bmatrix} Z \\ 0 \end{bmatrix} \tag{8}$$

$$K_{i,j} = \lambda \cdot \gamma^2 \cdot d_{i,j}^2 \ln d_{i,j} \tag{9}$$

$$\gamma = \frac{1}{n^2} \sum_{i=1}^{n} \sum_{j=1}^{n} d_{i,j}^2 \tag{10}$$

where K is an $N \times N$ matrix and P is an $N \times 3$ matrix, $p_i = [1\ x_i\ y_i]$ for the ith row. $Z = [z_1, z_2, \cdots, z_n]^T$. $d_{i,j} = \sqrt{(x_j - x_i)^2 + (y_j - y_i)^2}$. λ is the relative variance coefficient of the regularized item and is calculated as the ratio of the local variance and the global variance:

$$\lambda = \frac{\eta_{local}}{\eta_{global}} \tag{11}$$

$$\eta = \frac{\sigma}{\bar{s}} \tag{12}$$

where σ and $\bar{s}$ is the standard deviation of elevation and the mean saliency, respectively. Local variance η_{local} is calculated involving the points in the current grid while the global variance η_{global} is calculated involving all the points in the whole cluster. The influence of λ is illustrated in Figure 7.
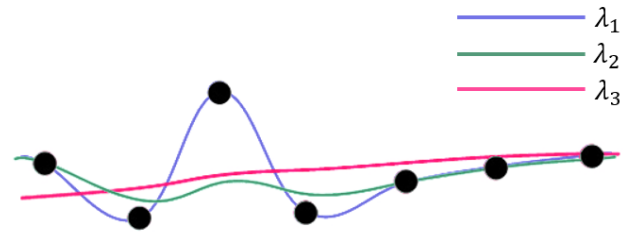

Figure 7. Surfaces using different λ fitting the same seed points. $\lambda_1 < \lambda_2 < \lambda_3$ and $\lambda_1 = 0$.

4. EXPERIMENTAL RESULTS

The software system for filtering was developed using Microsoft Visual Stdio 2015 under the Windows 7 x64 system with Intel core i5-4590 3.2Ghz CPU and 8G RAM. To verify the effectiveness and efficiency of the proposed SATPS algorithm, 10 test areas from 2 different airborne LiDAR datasets are selected and the characteristics of terrain environments are listed in Table 1. Area 1-9 come from Guangzhou dataset, each of which has 5 million points with a density of 10-20 pts/m². Each area size is 520m×460m, and the elevation is between 38m to 117m, and the average height of buildings is around 24m. The 10th area is from Las Vegas dataset, provided by USGS[1], which has more than 50 million points with a sparser density of 4-5 pts/m². The area size is 5380m×5350m, and the elevation is between 279.1m to 326.3m, while the average height of buildings is around 6m.

Area	Terrain characteristics	
	Topographic relief	Objects
1	smooth	buildings, vegetation, waterbody
2	smooth	complicated buildings, vegetation
3	smooth	complicated buildings, viaduct
4	smooth	complicated buildings, vegetation
5	sharp	buildings, waterbody, terrain fault
6	sharp	vegetation, buildings, viaduct
7	smooth	buildings and vegetation
8	sharp	buildings, power line, viaduct
9	sharp	slope, vegetation, steep, viaduct
10	smooth	buildings, vegetation

Table 1. Topological relief and main terrain types in test areas.

4.1 Quantitative results

The cross-matrices is used to evaluate the filtering results. Type I error the represents rejection of bare-earth points while Type II represents acceptance of points as bare-earth. The total error is the ratio of error classified points and the total points.

---

[1] USGS, https://viewer.nationalmap.gov/basic/#productSearch

Three state-of-the-art algorithms are selected as comparison including Progressive Morphological (PM) implemented by PCL[2], Progressive TIN Densification (PTD) in the commercial software TerraSolid, and Cloth Simulation Filtering (CSF) (Zhang et al., 2016). The quantitative results are listed in Table 2, and the bold fonts represent the lowest value of each error type among all the algorithms. The ground truth of all the points of Guangzhou dataset is annotated manually using TerraSolid software. And for the Las Vegas dataset, the DEM of 1m resolution provided along with the LiDAR dataset is used as reference.

Area	PM			PTD			CSF			SATPS		
	Type I	Type II	E_{Total}	Type I	Type II	E_{Total}	Type I	Type II	E_{Total}	Type I	Type II	E_{Total}
1	4.29	3.62	3.93	**3.45**	5.49	4.54	3.99	4.02	4.00	4.00	**3.15**	**3.55**
2	5.65	7.57	6.72	**3.17**	8.43	6.11	6.06	**6.46**	6.29	3.76	7.00	**5.57**
3	4.50	3.90	4.19	**2.01**	4.27	**3.19**	4.64	3.86	4.23	3.61	**3.12**	3.36
4	6.77	6.01	6.38	**3.34**	5.58	**4.50**	4.67	6.81	5.78	5.27	**5.11**	5.19
5	3.41	4.61	4.19	3.80	4.47	4.23	7.38	**3.89**	5.11	**3.31**	3.96	**3.73**
6	6.58	3.99	4.88	6.22	3.25	4.27	**2.92**	5.25	4.45	3.30	**3.24**	**3.26**
7	11.58	9.35	10.67	3.22	**9.09**	5.62	3.62	11.53	6.86	**1.23**	10.49	**5.01**
8	9.06	3.16	6.05	2.85	4.35	3.61	**2.29**	6.02	4.20	**2.11**	**2.85**	**2.49**
9	6.81	**3.34**	4.71	3.32	5.05	**4.37**	4.93	12.89	9.74	**1.62**	12.63	8.27
10	3.80	**12.70**	7.83	3.42	13.36	7.57	**2.23**	14.61	7.88	2.61	13.29	**7.50**
Mean	6.25	**5.83**	5.96	3.48	6.33	4.80	4.27	7.53	5.85	**3.08**	6.48	**4.79**

Table 2. Quantitative results of comparative methods.

The main parameters that affect the filtering results are the saliency threshold ε_h and $\varepsilon_{\gamma G}$. ε_h is used to calculate saliency and is set as 1m, which is reasonable for most urban scenes. $\varepsilon_{\gamma G}$ is used in candidate determination. $\varepsilon_{\gamma s}$ is used for *Scatter Ground* identification, and it can be simply set as same as $\varepsilon_{\gamma G}$ or slightly higher. The setting of $\varepsilon_{\gamma G}$ is related to the topography situation of the survey area. In areas with dense and complex ground buildings, such as urban areas, a smaller $\varepsilon_{\gamma G}$ value, 0.5, is used. In areas with sparse buildings or undulating terrain (rural or mountainous area), a larger $\varepsilon_{\gamma G}$ value, 0.75, is used. The terrains of two experimental area are flat, thus the $\varepsilon_{\gamma G}$ value is set to 0.5, and $\varepsilon_{\gamma s}$ is empirically set to 0.75. However, even if non-ground grids are not predicted correctly at the stage of saliency division, it is still available to filter the non-grounds using TPS interpolation but the time cost may increase sharply. According to the saliency and elevation variance, the variance coefficient η is smaller in smooth areas and larger with undulant topographic relief, which adapts the surface to complex terrains.

4.2 Qualitative results

The filtering results of site 1 and site 8 are displayed in Figure 8. In the original points, red represents buildings, green the vegetation, yellow the viaduct and pink for the ground. In the filtering results, yellow represents the non-ground points while pink for ground points. The terrain types in site 1 are relatively simple with smooth topological relief, which mainly includes buildings and vegetation. Site 9 is much more complex, which includes viaduct, slopes, buildings, and low vegetation. It can be seen that in most of the cases the filtering results are satisfying except for the low vegetation areas inside the circle. The boundaries of objects and grounds are confusing especially at the entrance of viaducts. Once the points grid is identified as non-ground points in saliency division, it is unavailable to be considered as ground and not enough candidate grid can be found

for the TPS fitting stage, which can be optimized by tuning the saliency thresholds.
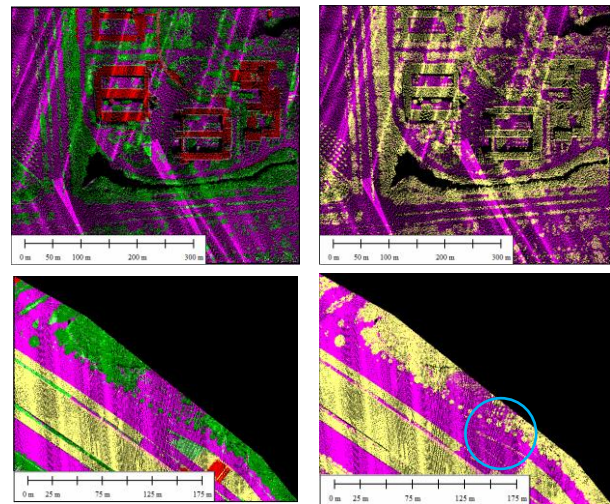
- 🟢 Low vegetation
- 🟢 High vegetation
- 🔴 Buildings
- 🟡 Non-ground points
- 🟣 Ground points

Figure 8. Filtering results from site 1 (top) and 9 (down). The left figures are the original point clouds rendered by classes and the right is the filtering results. (The areas without LiDAR coverage are shown as black in the pictures)

The DEM is generated from the ground points as shown in Figure 9. Compared to the other three algorithms, it is obvious that the proposed SATPS method performs better to filter building areas and preserve ground points inside the buildings at the same time, as shown in the red circle of Figure 9(d).

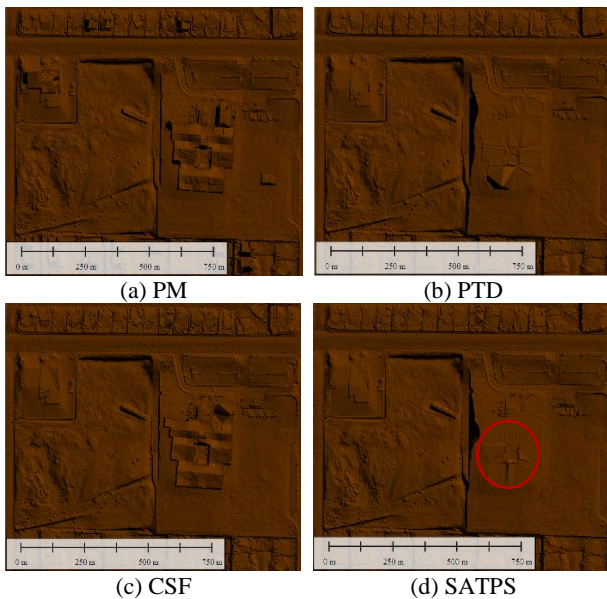[2] PCL, https://www.pointclouds.org/

(a) PM   (b) PTD

(c) CSF   (d) SATPS

Figure 9. DEM generation of Area 10 using filtering results.

4.3 Discussion

In most situations, PTD and the proposed SATPS algorithm achieve minimal Type I errors and the error rate is similar. The CSF performs well in flat areas but fails in a complex environment, the parameters are set specifically depending on the terrain structures, which cannot be uniformly set to the whole test area. In flat areas, the SATPS algorithm and CSF have minimal Type II errors while in complex scenes, the results of PTD and SATPS methods stand out. In building areas (Figure 10), PM and CSF consider the roofs as grounds.

(a) PM   (b) PTD

(c) CSF   (d) SATPS

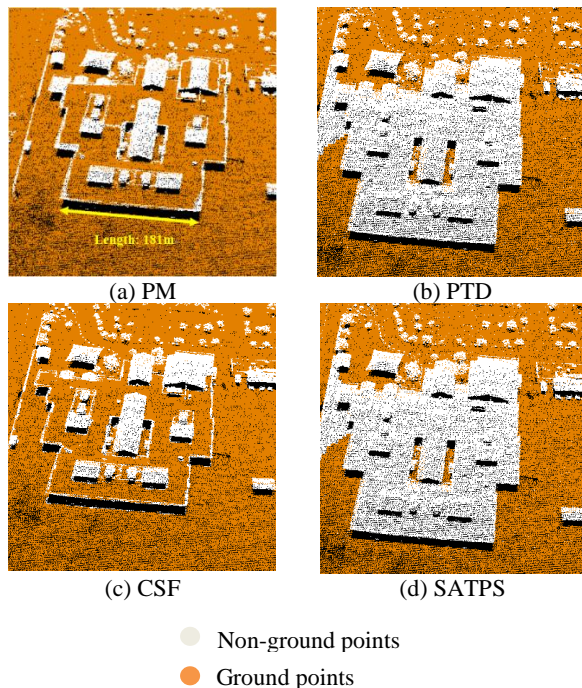○ Non-ground points

● Ground points

Figure 10. Comparative results of a building area in Area 10.

As for the total error rate, the proposed SATPS algorithm achieves the best results in more than half of the areas. The total error rate increases sharply when dealing with complicated

terrain environments. The results of PM are acceptable in flat areas but in the complex scenes, parameters should be precisely tuned for satisfying results, which is not adaptive enough.

Generally, the proposed filtering algorithm performs well in different terrain environments. Especially in complex scenes with hybrid structures, such as multi-layer buildings and bridges, the boundary is preserved and the vegetation can be separated clearly at the same time. Besides, the TPS interpolation is conducted by clusters and reduces the time cost evidently, which can meet the requirement for practical production. As shown in the last line of Table 2, the mean value of each error type calcuated from all the areas indicates that, the proposed SATPS algorithm performs better for Type I errors and total errors among all the four methods.

The SATPS algorithm combines ground saliency calculation and TPS interpolation to filter ground points. Compared with PTD, PM, CSF algorithms, large scale and global operations are avoided, thus the calculation is faster. Tested with point clouds of different point density, different terrain conditions, the proposed algorithm performs good adaptability. When dealing with complex and mixed terrain environment, it can still ensure that the error rate does not increase significantly.

5. CONCLUSIONS

To provide a feasible and efficient scheme for ground filtering in point clouds with complex or mixed terrains, a saliency-aware TPS interpolation method is proposed in this paper. Ground saliency is calculated for each 2D grid and with a saliency division strategy, potential ground grids are considered as candidate grid for seed point selection. To extract the ground surface, piece-wise TPS interpolation is conducted with a regularized item according to the saliency, which relaxes the constraints that TPS interpolates all the seed points rigorously. The parameters used in the algorithm are mostly adaptive and only few of them need to be tuned manually. The proposed SATPS algorithm achieved better performance in complex terrain structures compared to traditional methods. The grid segmentation and clustering results affect the seed point selection and TPS interpolation process, which can be further improved by supervoxel-based methods under the constraint of structural features and will be researched in the future works.

REFERENCES

Che, E. and Olsen, M.J., 2017. Fast ground filtering for TLS data via Scanline Density Analysis. *ISPRS Journal of Photogrammetry and Remote Sensing*, 129, pp. 226-240.

Chen, C., Li, Y., Yan, C., et al., 2016. An improved multi-resolution hierarchical classification method based on robust segmentation for filtering ALS point clouds. *International journal of remote sensing*, 37(4), pp. 950-968.

Cheng, P., Hui, Z., Xia, Y., Ziggah, Y.Y., Hu, Y. and Wu, J., 2019. An improved skewness balancing filtering algorithm based on thin plate spline interpolation. *Applied Sciences*, 9(1), p. 203.

Dong, Y., Cui, X., Zhang, L., et al., 2018. An Improved Progressive TIN Densification Filtering Method Considering the Density and Standard Variance of Point Clouds. *ISPRS International Journal of Geo-Information*, 7(10), pp. 409.

Gruszczyński, W., Puniach, E., Ćwiąkała, P., et al., 2019. Application of convolutional neural networks for low vegetation filtering from data acquired by UAVs. *ISPRS Journal of Photogrammetry and Remote Sensing*, 158, pp. 1-10.

He, Y., Zhang, C. and Fraser, C.S., 2018. Progressive filtering of airborne LiDAR point clouds using graph cuts. *IEEE Journal of Selected Topics in Applied Earth Observations and Remote Sensing*, 11(8), pp. 2933-2944.

Hu, H., Ding, Y., Zhu, Q., et al., 2014. An adaptive surface filter for airborne laser scanning point clouds by means of regularization and bending energy. *ISPRS Journal of Photogrammetry and Remote Sensing*, 92, pp. 98-111.

Hu, X., Ye, L., Pang, S. et al., 2015. Semi-global filtering of airborne LiDAR data for fast extraction of digital terrain models. *Remote Sensing*, 7(8), pp. 10996-11015.

Li, Y., Wu, H., Xu, H., et al., 2013. A gradient-constrained morphological filtering algorithm for airborne LiDAR. *Optics & Laser Technology*, 54, pp. 288-296.

Li, Y., Yong, B., Van Oosterom, et al., 2017. Airborne LiDAR data filtering based on geodesic transformations of mathematical morphology. *Remote Sensing*, 9(11), pp. 1104.

Liu, K., Wang, W., Tharmarasa, R., et al., 2019. Ground surface filtering of 3D point clouds based on hybrid regression technique. *IEEE Access*, 7, pp. 23270-23284.

Ma, W. and Li, Q., 2019. An Improved Ball Pivot Algorithm-Based Ground Filtering Mechanism for LiDAR Data. *Remote Sensing*, 11(10), pp. 1179.

Martínez Sánchez, J., Váquez Álvarez, Á., López Vilariño, et al., 2019. Fast ground filtering of airborne LiDAR data based on iterative scan-line spline interpolation. *Remote Sensing*, 11(19), pp. 2256.

Meng, X., Lin, Y., Yan, L., et al., 2019. Airborne LiDAR Point Cloud Filtering by a Multilevel Adaptive Filter Based on Morphological Reconstruction and Thin Plate Spline Interpolation. *Electronics*, 8(10), p. 1153.

Mongus, D. and Žalik, B., 2012. Parameter-free ground filtering of LiDAR data for automatic DTM generation. *ISPRS Journal of Photogrammetry and Remote Sensing*, 67, pp. 1-12.

Nie, S., Wang, C., Dong, P., et al., 2017. A revised progressive TIN densification for filtering airborne LiDAR data. *Measurement*, 104, pp. 70-77.

Qi, C.R., Su, H., Mo, K., et al., 2017. Pointnet: Deep learning on point sets for 3d classification and segmentation. In Proceedings of the IEEE Conference on Computer Vision and Pattern Recognition, pp. 652-660.

Qin, L., Wu, W., Tian, Y., et al., 2017. LiDAR filtering of urban areas with region growing based on moving-window weighted iterative least-squares fitting. *IEEE Geoscience and Remote Sensing Letters*, 14(6), pp. 841-845.

Rizaldy, A., Persello, C., Gevaert, C., et al., 2018. Ground and multi-class classification of airborne laser scanner point clouds using fully convolutional networks. *Remote Sensing*, 10(11), pp. 1723.

Roberts, K.C., Lindsay, J.B. and Berg, A.A., 2019. An Analysis of Ground-Point Classifiers for Terrestrial LiDAR. *Remote Sensing*, 11(16), pp. 1915.

Susaki, J., 2012. Adaptive slope filtering of airborne LiDAR data in urban areas for digital terrain model (DTM) generation. *Remote Sensing*, 4(6), pp. 1804-1819.

Wan, P., Zhang, W., Skidmore, A.K., et al., 2018. A simple terrain relief index for tuning slope-related parameters of LiDAR ground filtering algorithms. *ISPRS Journal of Photogrammetry and Remote Sensing*, 143, pp. 181-190.

Wang, T., Li. J., An, X. 2015. An Efficient Scene Semantic Labeling Approach for 3D Point Cloud[C]// IEEE International Conference on Intelligent Transportation Systems. IEEE.

Yang, B., Huang, R., Dong, Z., et al., 2016. Two-step adaptive extraction method for ground points and breaklines from lidar point clouds. *ISPRS Journal of Photogrammetry and Remote Sensing*, 119, pp. 373-389.

Yilmaz, V., Konakoglu, B., Serifoglu, C., et al., 2018. Image classification-based ground filtering of point clouds extracted from UAV-based aerial photos. *Geocarto International*, 33(3), pp. 310-320.

Zeybek, M. and Şanlıoğlu, İ., 2019. Point cloud filtering on UAV based point cloud. *Measurement*, 133, pp. 99-111.

Zhang, W., Qi, J., Wan, P., et al., 2016. An easy-to-use airborne LiDAR data filtering method based on cloth simulation. *Remote Sensing*, 8(6), pp. 501.

Zhao, X., Guo, Q., Su, Y., et al., 2016. Improved progressive TIN densification filtering algorithm for airborne LiDAR data in forested areas. *ISPRS Journal of Photogrammetry and Remote Sensing*, 117, pp. 79-91.